Experimental Composition of Two Systems: Ring Resonator Structures and Y-Shaped Demultiplexer

THESIS

Presented to the Faculty of the Department of Physics and Astronomy
in Partial Fulfillment of the Major Requirements
for the Degree of

BACHELOR OF SCIENCE IN
PHYSICS

Carina Noemi Vazquez Nunez

May 2022

Experimental Composition of Two Systems: Ring Resonator Structures and Y-shaped Demultiplexer

Carina Noemi Vazquez Nunez

Signature of Author:

_____

Department of Physics and Astronomy
May 2022

Certified by:

_____

Dr. William Robertson
Professor of Physics & Astronomy
Thesis Supervisor

Accepted by:

_____

Dr. Ronald Henderson
Professor of Physics & Astronomy
Chair, Physics & Astronomy

ABSTRACT

In this work, we experimentally investigated two acoustic systems: the Y-shaped demultiplexer and the acoustic ring resonator. The first experiment was a demultiplexer which separates and transmits specific frequencies from a broadband input signal. The acoustic demultiplexer investigated here is based on resonances created by side-attached waveguide stubs. The Y-shaped waveguide sent broad bandwidth sound along an input line. Two output lines with a stub filter arrangement transmitted narrow bands of two different frequencies separated from the broadband input. The second set of experiments concerned ring resonators which are widely used in optics as filters and switches. Here we investigated the acoustic analog to the optical ring resonator. Three specific ring resonators systems are demonstrated: a simple single ring structure that acts as a comb filter, a single ring between two parallel waveguides that acts as an add-drop filter, and a sequential array of equally spaced rings that creates acoustic band gaps. The acoustic ring resonators consist of a circular waveguide attached tangential to a straight waveguide. The ring waveguide has resonances whenever the path around the ring equals an odd half-integer multiple of the wavelength. We showed that this phenomenon can be used to create notch filters, add-drop filters, and broad acoustic bandgap reflectors. The experiments are conducted in linear waveguides using an impulse response method. The ring resonators were created via 3D printing. Finite-element numerical simulations were conducted using COMSOL Multiphysics software. The experimental results were in good agreement with numerical models rendered in python and finite-element simulations.

TABLE OF CONTENTS

LIST OF FIGURES

I. INTRODUCTION

This thesis explores two acoustic configurations: a Y-shaped demultiplexer and a series of ring resonator structures were explored in order to study each of their wave manipulating properties. Both structures can be considered as different forms of wave filters. There are three phases to the research on each systems. First, I created a python program to compute the theoretical sound transmission in a simple ring resonator and y-shaped demultiplexer. Second, in collaboration with MTSU's REU program, we used COMSOL Multiphysics to model ring resonator structures and Y-shaped demultiplexer. Three different ring resonator structures were investigated specifically a simple ring resonator, an add-drop filter, and an array of eight ring resonators. Third, I needed to build the experimental set-ups based on the theoretical papers for the optical ring resonator and acoustic demultiplexer. I was able to do this using PVC pipes as waveguides and 3D printed parts.

The first system investigated considered the use of acoustic ring waveguides as resonant elements in comb/notch filters, add-drop filters, and acoustic band gap arrays. The results offer insight into the interference mechanism of ring resonators in both time and frequency. Experiments in Python and simulations using COMSOL Multiphysics software are performed at audio frequencies from 100 Hz to 3500 Hz. The 3D printed ring resonators are sized such that the frequency test range begins below the lowest resonant frequency of the ring. By demonstrating close agreement between experimental results and finite-element numerical modeling through

COMSOL, we were able to show that simulation is an effective method of evaluating meta-material structures that are too complicated to test exhaustively through experimentation.

The second system examined presents the results of an experimental and computational study of a Y-shaped acoustic waveguide demultiplexer described recently in an analytic theory by Mouadili et al. [3]. The Y-shaped waveguide consists of one input and two output lines. Broad bandwidth sound incident along the input line is largely reflected from the Y-junction except for two different frequency bands which are selectively directed one along each output arm of the Y. The operation of the demultiplexer is based on narrow frequency transmission bands along each arm of the Y due to Fano resonances created by strategically placed waveguide stubs. The stub resonances are selected such that the Fano resonance occurs between two transmission minima leading to a narrow transmission band that creates so-called acoustic induced transparency. For the waveguide and stub parameters used in our experiment we examine the predicted response of the analytic theory. The theory is then compared to finite-element simulations conducted using COMSOL. Finally, experimental results of the audio frequencies are presented using an impulse response method and a direct demonstration of pulse demultiplexing.

II. RING RESONATOR STRUCTURES
A. Analytic Theory

Using the analytic theory in the paper by Rabus's [1], I was able to write a Python code simulation program that predict graphs of the frequency domain transmission for simple configurations of a ring resonator. The basic configuration of a ring resonator consists of unidirectional coupling between a ring resonator with radius r and a waveguide, is described in Figure 1.

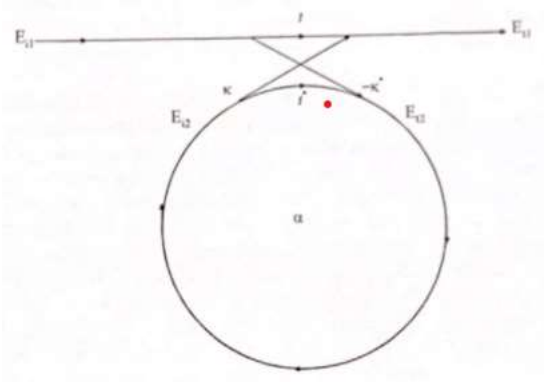

FIGURE 1: Model of a single ring resonator with one waveguide.

I was able to model this using the interaction of the unidirectional coupling between the ring resonator and the tangential waveguide that is described by the matrix relation [1]:

$$\begin{pmatrix} E_{t1} \\ E_{t2} \end{pmatrix} = \begin{pmatrix} l & \kappa \\ -\kappa^* & t^* \end{pmatrix} \begin{pmatrix} E_{i1} \\ E_{i2} \end{pmatrix} \quad (1)$$

The complex mode amplitudes E are normalized, so that their squared magnitude corresponds to the modal power. The coupler parameters t and k depend on the specific coupling mechanism used. The * denotes the conjugated complex value of t

and k, respectively.[1]

The matrix is symmetric because the networks under consideration are reciprocal. Therefore,

$$|\kappa^2| + |t^2| = 1. \quad (2)$$

In order to further simplify the model E_{i1} is chosen to be equal to 1. Then the round trip in the ring is given by

$$E_{i2} = \alpha \cdot e^{i\theta} E_{t2}, \quad (3)$$

Where α is the loss coefficient of the ring and $\theta = \frac{\omega L}{c}$, L being the circumference of the ring which is given by $L = 2\pi r$, r being the radius of the ring measured from the center of the ring to the center of the waveguide, c is the phase velocity of the ring mode $\left(c = \frac{c_o}{n_{eff}}\right)$ and the fixed angular frequency $\omega = kc_o$, c_o refers to the vacuum speed of light. The vacuum wavenumber k is related to the wavelength λ through: $k = \frac{2\pi}{\lambda}$. Using the vacuum wavenumber, the effective refractive index n_{eff} can be introduced easily into the ring coupling relations by

$$\beta = k \cdot n_{eff} = \frac{2\pi \cdot n_{eff}}{\lambda}, \quad (4)$$

where β is the propagation constant. This leads to

$$\theta = \frac{\omega L}{c} = \frac{k c_o L}{c} = k \cdot n_{eff} = \frac{2\pi \cdot n_{eff} \cdot 2\pi r}{\lambda} = 4\pi^2 n_{eff} \frac{r}{\lambda} \quad (5)$$

From (2) and (3) we obtain

$$E_{t1} = \frac{-\alpha + t \cdot e^{-j\theta}}{-\alpha t^* + e^{-j\theta}}, \quad (6)$$

$$E_{i2} = \frac{-\alpha\kappa^*}{-\alpha t^* + e^{-j\theta}}, \qquad (7)$$

$$E_{t2} = \frac{-\kappa^*}{1 - \alpha t^* e^{j\theta}} \qquad (8)$$

This leads to the transmission power P_{t1} in the output waveguide, which is

$$P_{t1} = |E_{t1}|^2 = \frac{\alpha^2 + |t|^2 - 2\alpha|t|\cos(\theta + \varphi_t)}{1 + \alpha^2|t|^2 - 2\alpha|t|\cos(\theta + \varphi_t)} \qquad (9)$$

Where $t = |t|\exp(j\varphi_t)$, $|t|$ representing the coupling losses and φ_t the phase of the coupler.

The circulating power P_{i2} in the ring is given by

$$P_{i2} = |E_{t2}|^2 = \frac{\alpha^2(1 - |t|^2)}{1 + \alpha^2|t|^2 - 2\alpha|t|\cos(\theta + \varphi_t)} \qquad (10)$$

On resonance, $(\theta + \varphi_t) = 2\pi m$, where m is an integer, the following is obtained:

$$P_{t1} = |E_{t1}|^2 = \frac{(\alpha - |t|^2)^2}{(1 - \alpha|t|)^2} \qquad (11)$$

and

$$P_{i2} = |E_{i2}|^2 = \frac{\alpha^2(1 - |t|^2)}{(1 - \alpha|t|)^2} \qquad (12)$$

A special case happens when $\alpha = |t|$ in (11), when the internal losses are equal to the coupling losses. The transmitted power becomes 0. This is known as critical coupling, which is due to destructive interference. [1]

In using the above equations, I was able to model the behavior of a simple ring resonator filter configuration consisting of only one waveguide and one ring. The wavelength-dependent filter characteristic for a ring resonator with a radius of $r = 148\ \mu m$ with matched coupling and loss coefficient, derived using (1)-(11), is

shown in Figure 2.

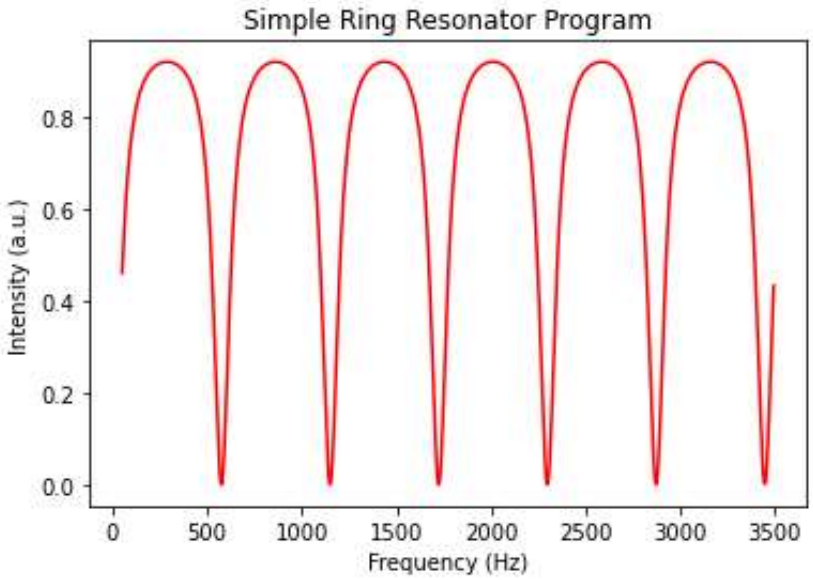

FIGURE 2: Transmission intensity for a single ring resonator.

Using this model, I can modify the code so that it models acoustic phenomena. This is essentially accomplished by replacing the speed of light by the speed of sound and by using appropriate waveguide and ring dimensions. In this manner the theory could be extended to suit the requirement of various types of ring resonator configurations such as the add-drop structure and the array experiments.

B. Experimental Configuration

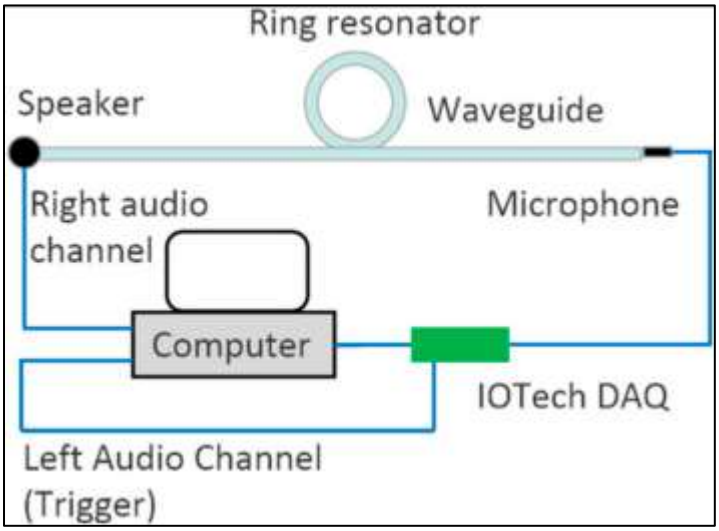

FIGURE 3: Schematic of the impulse response system used to measure the response of ring resonator configurations.

A schematic of the experimental arrangement for ring resonator experiments is shown in Figure 3, which illustrates the measurement of a single resonator structure. A small speaker and a microphone were located at opposite ends of a 12 m long section of a 2.0 cm diameter cylindrical acoustic waveguide made from a PVC pipe. The sample under test, a single ring structure in the Figure 3, was located in the center of this 12 m long waveguide test bed. A computer sound card with stereo output was used to generate a short audio impulse on the right channel and a square trigger signal on the left channel. The impulse signal was directed to a speaker (Apple M8756G/A) and the trigger signal to one analog-to-digital (AD) port of an IOTech DAQ/3000 data acquisition module. The IOTech DAQ/3000 was USB connected to the computer, and, with each impulse, the audio signal transmitted to the microphone

(Aco Pacific 7012) was digitally acquired at a second AD port. The use of triggered acquisition meant that each subsequent recorded impulse could be added and averaged coherently to the previous signals leading to time-domain data with a very high signal-to-noise ratio. Typical runs used 250 averaged signal acquisitions. For more accurate measurement some runs used 1000 averaged signal acquisitions.

The ring resonators were 90 mm radius toroidal waveguides for the single ring experiments, 80 mm radius toroids for the add-drop structure, and 45 mm for the array experiments. The inner opening diameter of the toroids was 2.0 cm to match that of the 12 m long waveguide test bed. The ring waveguide was attached to a tangential section of a straight waveguide as shown in Figure 4.

FIGURE 4: Two views of the ring resonator structure. In all rings used in these experiments, the inner opening diameter was 2.0cm. For the single ring results, the ring radius was 9.0 cm to the centerline of the circular waveguide. For the add-drop experiments, the ring diameter was 8.0cm. For the ring array, the diameter is 4.5 cm. The lower figure illustrates the opening that connected the ring and straight waveguides.

A small hole coupled the straight waveguide segment to the ring waveguide as can be seen in the lower image in Figure 4. The ring resonators were designed in Autodesk Fusion 360 and then constructed in polylactic acid (PLA) using a Prusa MK3 3D printer.

C. Finite Element Simulation

The three ring resonator configurations explored experimentally were also simulated numerically using finite element analysis using COMSOL. The COMSOL simulations were done in collaboration with Jennifer Lopez and Alex LaVerde who were at MTSU as part of an NSF REU program in Computational Science. A 3D model of the system was created as shown in Figure 5.

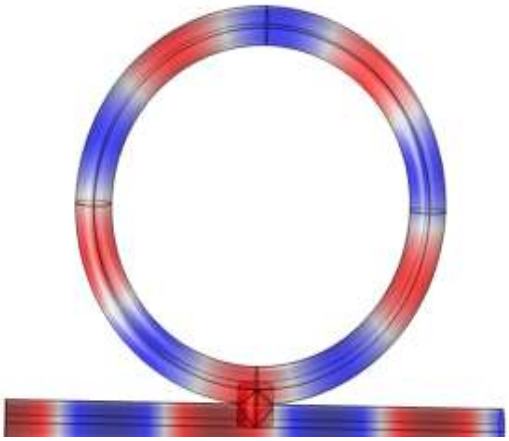

FIGURE 5: Pressure plot of the single ring resonator.

The structures were modeled using hard reflecting surfaces for the ring and straight waveguide segments. The input was a plane wave with a pressure amplitude of 0.2 Pa that was swept across a frequency range of 4000 Hz in steps of 2 Hz. The impedance matched output eliminated end reflections meaning that the simulation did not need to implement a long waveguide as in the actual experiment. The simulation output was determined by integrating across the surface of the output port of the waveguide. The signals were normalized by dividing the output of a ring resonator structure with that of a straight reference waveguide.

D. Data Analysis

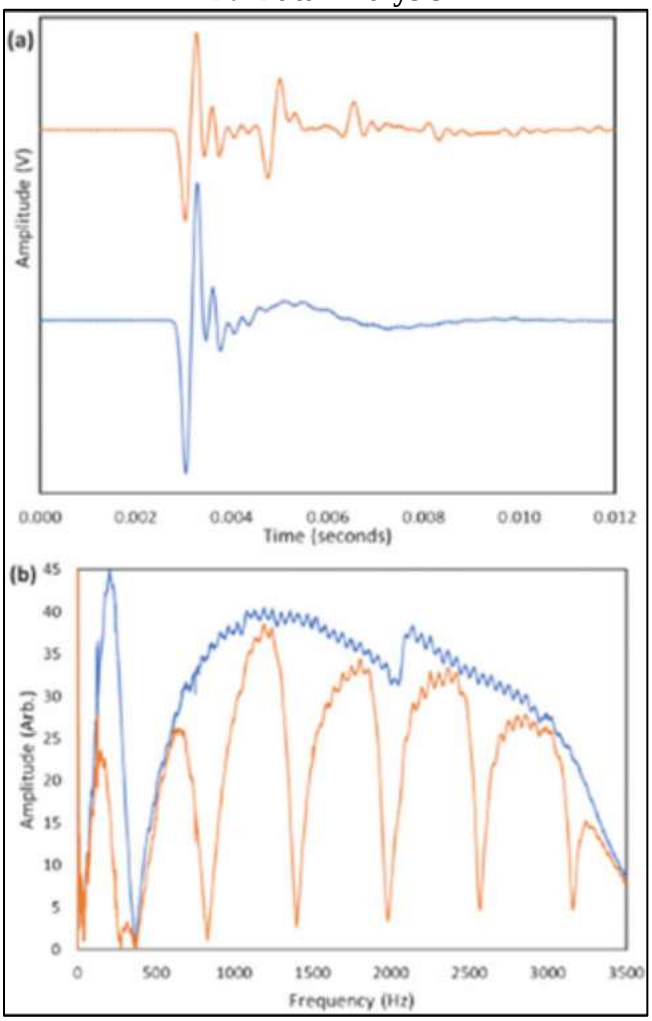

FIGURE 6: (a) Time-domain measurement of the reference signal through a straight waveguide (lower plot in blue) and the time signal with a single side-loaded ring resonator (offset upper plot in orange). (b) Fourier transforms of the time signals shown in (a) indicating the comb filtering response of the ring resonator.

Before setting up each of the ring resonator structures, I would take a reference signal as shown in blue on Figure 6a by averaging hundreds of pulses down the straight pipe. To obtain signals with high signal-to-noise we use the add and average method, where after each pulse we add the measurements together and then

divide by the number of pulses which reinforces the desired signal and averages out random noise. The time domain data is converted to the frequency domain using a numerical Fourier Transform as shown in Figure 6b. Examples of time-domain data through a straight waveguide and through a waveguide with a single attached ring resonator are shown in Figure 6a. Numerical Fourier transforms were used to convert the time-domain data to the frequency domain. The frequency resolution of the Fourier transform (1 Hz) is limited by the need to truncate the acquired signal to eliminate back reflections from the ends of the waveguide. The 12 m long test bed assured that there was sufficient time before the first reflection to achieve good frequency resolution. [5] The use of the straight waveguide data to normalize the ring filter signal results in the transmission function of the ring structure alone, independent of loss, phase change, or detector response in the lead-in or lead-out waveguide system. The loss in the waveguides in this frequency range is small, and, because the ring waveguides are short, waveguide losses are negligible.

E. Filtering by a Single Ring Resonator

The filtering properties of a single ring resonator were measured experimentally using the arrangement shown schematically in Figure 3. The time-domain data for the transmission with a single ring are shown as the upper plot in Figure 6a. The initial impulse is followed by a periodic sequence of delayed pulses that correspond to signals traveling around the loop one or more times before continuing down the waveguide. The lower plot in Figure 6a shows a reference impulse signal through a straight waveguide. Figure 6b shows the results of Fourier transforming the time signals from Figure 6a. The reference spectrum (blue) shows that the impulse contains frequency components out past 3500 Hz. The spectrum with the single ring resonator shows the periodic filtering pattern commonly referred to as comb or notch filtering with periodic sharp drops in transmission. The reference spectrum shows one notable experimental limitation in that the speaker and impulse combination led to a sharp drop in transmission at about 400 Hz. In some subsequent presentations of experimental results, the small frequency interval around 400 Hz is eliminated.

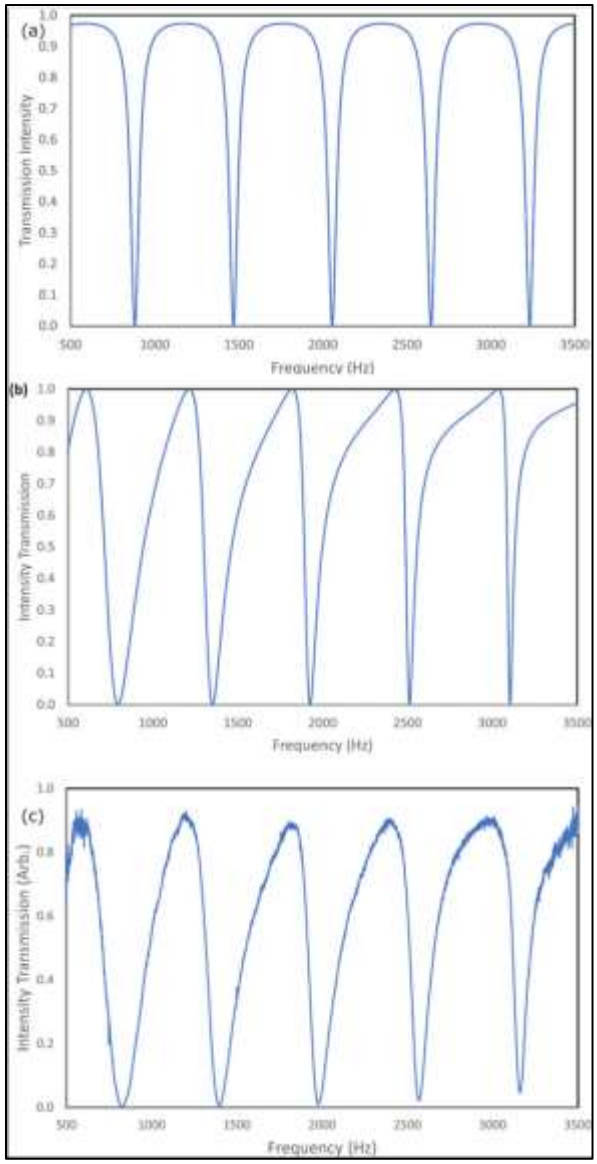

FIGURE 7: Transmission intensity for a single ring resonator: (a) simple analytic theory, (b) finite element simulation, and (c) experimentally measured intensity transmission.

To obtain the normalized intensity transmission, the Fourier transform of the signal is divided by that of the reference and the result squared. The outcome of this process for the experimental data from Figure 6 is shown in Figure 7c. For

comparison, Figure 7a shows an analytical prediction based on a simple generic ring resonator theory by Rabus.[1] The transmitted power is

$$P = \frac{\alpha^2 + |t|^2 - 2\alpha|t|\cos(\theta + \varphi_c)}{1 + \alpha^2|t|^2 - 2\alpha|t|\cos(\theta + \varphi_c)}$$

where α is the loss coefficient of the ring, $\theta = \omega L/v$, with L being the ring circumference and v the speed of sound in air, and t and ϕ_c are the coupling loss magnitude and phase, respectively. The critical coupling case in which $\alpha = t$ describes pure destructive interference and is used to generate Figure 7a. The result is a series of symmetrical notch filter profiles that accurately describes the frequency of the minima using a coupling phase corresponding to the 2 cm offset of the tangential ring. However, the asymmetrical line shape of the experimental result is not captured by this simple analytic result. In contrast, the finite element result from COMSOL plotted in Figure 7b accurately replicates both position and line shape. The depths of the minima are not as deep experimentally as predicted numerically. However, the finite element simulation assumes no loss. In the past work on curved acoustic waveguides, we found that there is a small curvature-induced attenuation that becomes larger with increasing frequency. This result is consistent with incomplete destructive interference between the waveguide and ring signals.

The acoustic ring resonator results provide insights into the mechanism and behavior of other ring resonators that is not accessible with their more frequently studied optical counterparts. From the upper time-domain plot in Figure 6a, the interval between the successive pulses is 1.73 ms, which, with a speed of sound of

344 m/s, gives a value of 0.59 m for the ring path length. The ring circumference measured down the centerline of the ring waveguide is L = 0.57 m.

In the frequency-domain data of Figure 6b, the first resonant transmission minimum occurs at a frequency of 274 Hz corresponding to a wavelength of 1.255 m. This value is slightly higher than twice the ring centerline path length of 1.14 m, indicating that the lowest frequency minimum corresponds closely to the half-wavelength destructive interference. The higher frequency transmission minima (832, 1385, 1956, 2569, and 3162 Hz) are all odd multiples of the lowest frequency, and thus, the minima correspond closely to wavelengths $m\frac{\lambda}{2} = L$, where *m* is an odd integer.

Both the time and frequency domains indicate that the effective path appears larger than the physical path length, L, of the centerline of the ring. This effect is likely due to the distance 0.02 m between the ring centerline and that of the straight waveguide. In optical ring resonators, this difference is typically referred to as the coupling phase.[1]

F. Add-Drop Filter

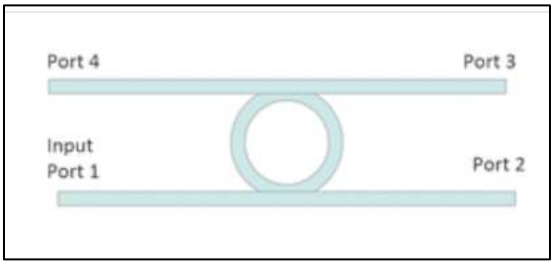

FIGURE 8: Add-drop filter configuration using an acoustic ring resonator. The input signal at port 1 is channeled into ports 2, 3, and 4 as shown in the transmission profile.

In optics, the ring resonator structure is often employed as an add-drop filter in which particular frequencies are switched between ports to realize wavelength division multiplexing and demultiplexing. The arrangement of the acoustic add-drop filter investigated here is shown in Figure 8. In the experimental realization, the two parallel waveguides were 12 m long with a single 80 mm radius ring attached between the guides.

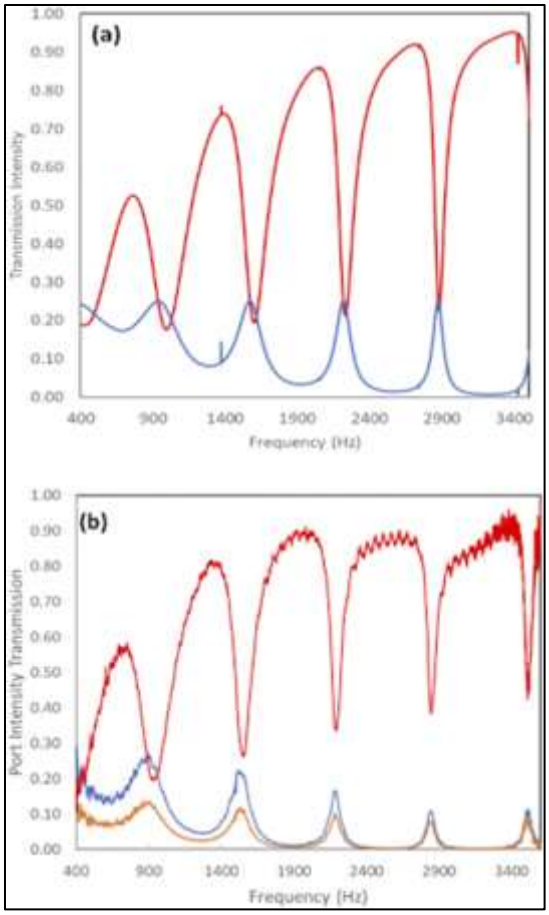

FIGURE 9: (a) COMSOL simulation of the transmission to each port in a ring resonator add-drop filter. The upper plot (red) is transmission to port 2. The transmission is equal in ports 3 and 4 (overlapping blue plot). (b) Experimental measurement of the transmission. The upper curve (red) is transmission to port 2, the curve below (blue) is transmission to port 3, and the lowest plot (orange) is transmission to port 4.

Figure 9a shows the results of finite element simulation of the system. The uppermost trace (red) in the figure shows the transmission from the input to port 2. As with the single ring, there are a series of transmission dips corresponding to destructive interference in the lower waveguide. At the frequency of the dips, sound is directed to the other two ports in the second upper waveguide. In the simulation,

the intensity at ports 3 and 4 is equal with the value shown by the lower trace (blue) in Figure 9a.

To acquire experimental data, the audio speaker was connected at port 1. Impulse response measurements were recorded in separate experiments moving the microphone between ports 2, 3, and 4. A reference pulse was acquired by transmission through a 12 m long straight waveguide between ports 1 and 2. Using the same Fourier analysis method, the normalized transmission into each port is shown in Figure 9b. The results are in generally good agreement with the simulation. The sound coupled to ports 3 and 4 is not equal as in the simulated data; rather, there is slightly higher intensity in port 3.

G. Linear Ring Arrays

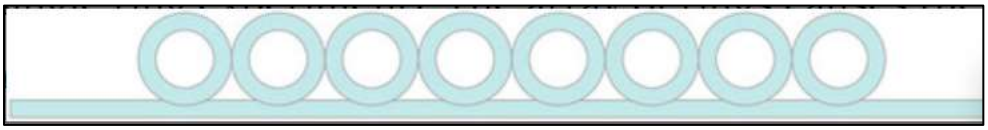

FIGURE 10: Configuration of the eight-ring linear array.

To explore a novel and more complicated structure, a regular linear array of equally spaced ring resonators was simulated in COMSOL. The configuration is shown schematically in Figure 10. The rings in this case were smaller than in the previous systems (45 mm radius), and the system considered a series of eight rings with an inter-ring spacing of 141 mm. The results of simulation are shown in Figure 11a. The lowest resonance of a single ring is just above 500 Hz (approximately twice the frequency of the 90 mm radius ring used in the single ring experiment). The coherent interference of the regular array of rings causes the bandgap of the single notch filter profile to be broadened considerably. The eight-ring array creates bandgaps from 400 to 745 Hz, 1610 to 1875 Hz, and 2905 to 3060 Hz.

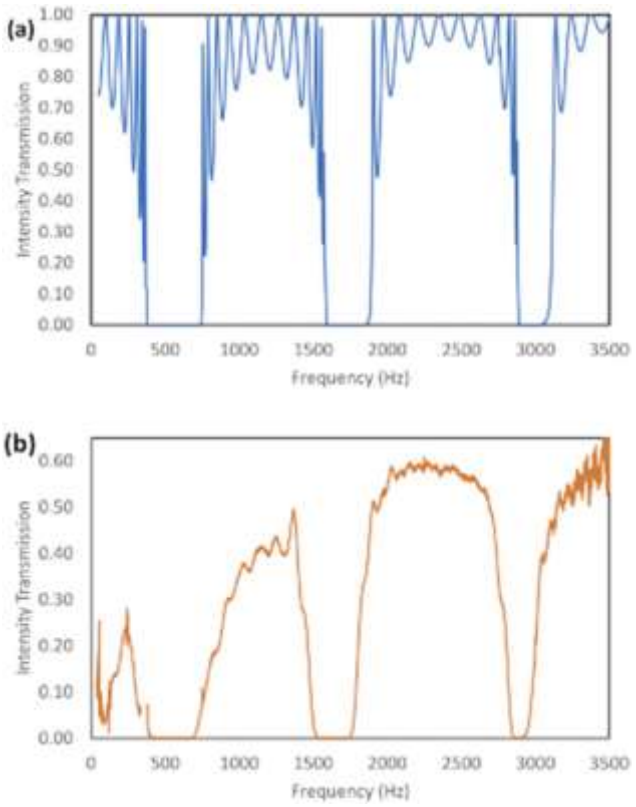

FIGURE 11: Transmission through a linear array of eight equally spaced ring resonators: (a) COMSOL simulation and (b) experiment.

The impulse response measurements were conducted by acquiring a signal through the 12 m waveguide test bed with the eight-ring array and a reference through a 12 m straight waveguide. The intensity transmission shown in Figure 11b is in generally excellent agreement with the simulation.

H. Experimental Results

In all cases, there was generally excellent agreement between the finite element simulation and the experimental results as shown in Figure 7. For the simple ring resonator, the simulation and experimental results show that the band-gap is much wider at lower frequencies than the analytic theory results predict. This is because the coupling parameters constant in the analytic theory, while the others accurately reflect that the coupling parameters are dependent on the frequency coming through. For the add-drop filter, the experimental results show a small difference in the two transmittance guides, which is not present in the simulation results. This comes from the simulation losing directional data for the wave propagation as it enters the resonator. The experimental data reflects how the waves traveling counter-clockwise would be more likely to exit via the drop port. The demonstrated good agreement with simulation means that more complicated structures can be modeled with confidence such as the linear array rings experiment. A wealth of follow-on simulations can be contemplated, such as double or triple ring add-drop filters, borrowing ideas from the optical ring resonator world. The behavior of linear ring arrays opens up a number of interesting options. Arrays with missing rings should create defect states within the bandgap, rings of slightly varying diameters could be designed to create broader bandwidth gaps, and rings with sub-wavelength spacing may give rise to interesting meta-material effects.

I. Conclusion

This work demonstrated the ring waveguide as a versatile resonant element in manipulating the waveguide transmission of audio frequency sound waves. The single ring results illustrate the basic mechanism of ring resonators based on half-wavelength destructive interference between the ring and waveguide signals. The add-drop filter demonstrates the ability to perform wavelength division multiplexing of audio signals. Finally, the use of linear ring arrays makes possible high-attenuation bandgaps with a broad frequency bandwidth. The results of this work were published in AIP Advances [6]

III. Y-SHAPED DEMULTIPLEXER

A. Y-shaped Demultiplexer

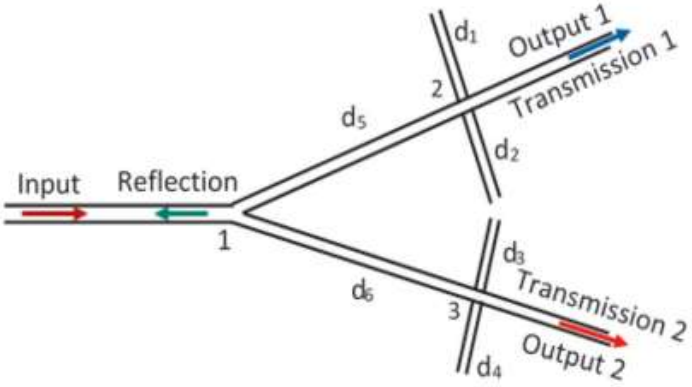

FIGURE 12: Schematic representation of a Y-shaped demultiplexer with one input line and two output lines. Two stubs are grafted at the same position along each output line.

The acoustic waveguide structure shown in Figure 12 was predicted theoretically to act as a demultiplexer by Mouadili et al. [3]. Originally, we interpreted that the two stubs on each side were open end waveguide stubs, however, upon early exploration we realized that they need to be closed end waveguide stubs. The schematic shown in Figure 12 is composed of an input line and two output lines, all fixed at point 1. The first output line contains two stubs of lengths d_1 and d_2 inserted on the same site 2 at a distance d_5 from the input 1. Likewise, the second output line contains two stubs of lengths d_3 and d_4 inserted on the same site 3 at the distance d_6 from the input 1. In a cross structure, the AIT resonance is obtained by the entire stub of lengths $d_0 = d_1 + d_2$. This resonance is trapped between two transmission zeros induced by the two elementary stubs of length d_1 and d_2. The calculation of the transmission and reflection coefficients was carried out using the

Green's function method [2]. For simplicity, all waveguides are assumed being characterized by the same characteristic impedance $Z = \frac{\rho v}{S}$ where ρ = 1.2 Kg/m^3 and v = 342 m/s are respectively the density and velocity of the fluid inside the slender tubes and S = 3.14 cm^2 is the section of the guide.

The analytical expressions of the transmission coefficients t_1 and t_2 along first and second output lines and the reflection coefficient r in the input line are obtained using the same procedure of calculation as for photonic waveguides [3].

The expressions of t_1, t_2 and r in closed form, namely

$$t_1 = \frac{2C_1C_2(-C_6C_3C_4 + S'S_6 + jC_3C_4S_6)}{X_1 + jX_2} \quad (13)$$

$$t_2 = \frac{2C_3C_4(-C_5C_1C_2 + SS_5 + jC_1C_2S_5)}{X_1 + jX_2} \quad (14)$$

And

$$r = -\frac{\xi_1 + j\xi_2}{X_1 + jX_2} \quad (15)$$

Where

$$\xi_1 = C_1C_2C_3C_4(S_5S_6 - C_5C_6) + C_1C_2S'C_6S_5 + C_3C_4SC_5S_6 + SS'S_5S_6 \quad (16)$$

$$\xi_2 = C_1C_2C_3C_4S_0 + C_1C_2S'C_5S_6 + C_3C_4SC_5S_6 - S_0SS' \quad (17)$$

$$X_1 = 3C_1C_2C_3C_4(S_5S_6 - C_5C_6) + C_1C_2S'(S_0 + C_5S_6) + C_3C_4S(S_0 + C_6S_5) - SS'S_5S_6 \quad (18)$$

$$X_2 = C_1C_2C_3C_4(3C_6S_5 + 3C_5S_6) + (C_5C_6 - 2S_5S_6) + (C_1C_2S' + C_3C_4S) - S_0SS' \quad (19)$$

and $C_i = \cos(kd_i)$, $S_i = \sin(kd_i)$ (i = 1-6), $S = \sin(k(d_1 + d_2))$, $S' = \sin(k(d_3 + d_4))$, $S_0 =$

$\sin(k(d_5 + d_6))$. $k = \omega/v$ is the wave-vector of the sound wave in the slender tubes and ω is the angular frequency. [4]

The foregoing theoretical model proposed by Mouadili et al. provides analytic expressions for the complex frequency dependent amplitude transmission down each arm (t_1 and t_2) and the reflection amplitude back along the input arm (r). The condition for transmission maxima along each output arm at neighboring frequencies leads to the defining conditions on the lengths $d_1 – d_6$:

$$d_1 = \frac{d_0}{2} - \frac{\delta}{2} \qquad (20)$$

$$d_2 = d_5 = \frac{d_0}{2} + \frac{\delta}{2} \qquad (21)$$

$$d_3 = d_6 = \frac{d_0}{2} \qquad (22)$$

$$d_4 = \frac{d_0}{2} + \delta \qquad (23)$$

where $d_0 = d_1 + d_2$ and $\delta = d_2 - d_1 \neq 0$ is a detuning factor. The expressions for t_1, t_2, and r were coded in python enabling plots of frequency versus the transmitted and reflected intensities $T_1 = |t_1|^2$, $T_2 = |t_2|^2$, and $R = |r|^2$. To verify that our code was correct we used the example values used to create Figure 2 in the source work[4] of $d_0 = 8.57$ cm and with δ taking on values of 1.85 cm, -1.85 cm, 1.13 cm, and -1.13 cm this is shown in Figure 13.

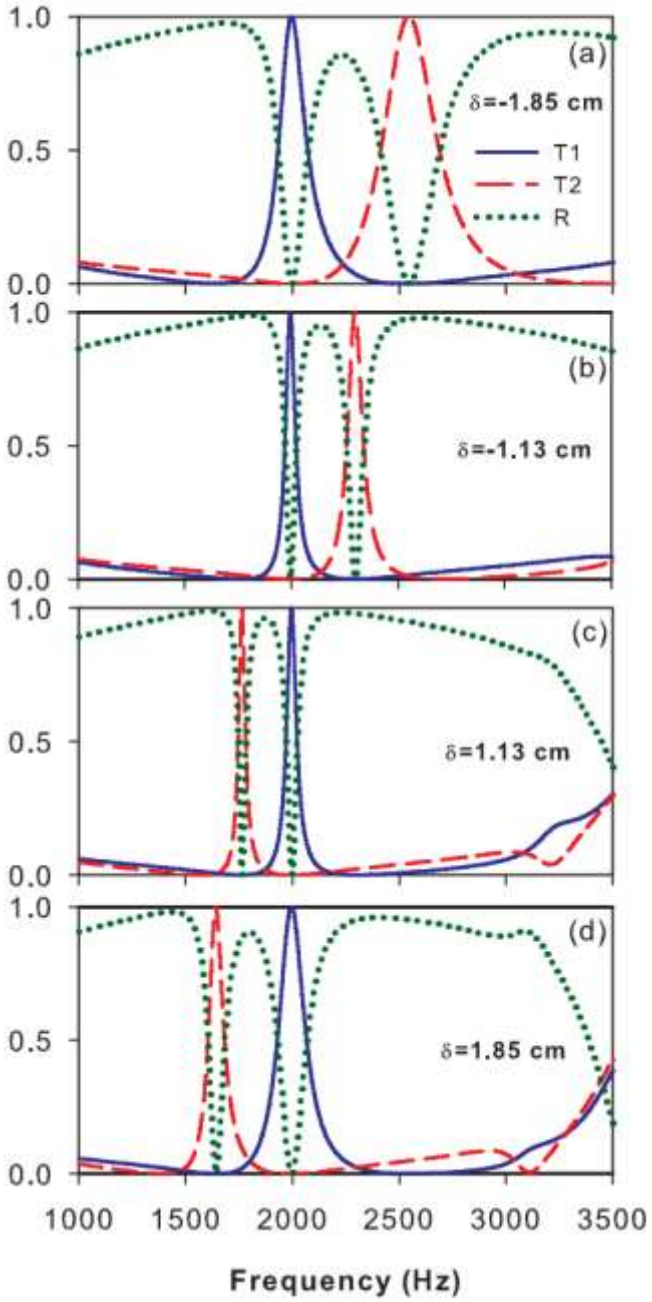

FIGURE 13: From Mouadilli's article Figure 2: Variation of the transmission along the output 1 (continuous curve), the output 2 (discontinuous curve) and the reflection in the input (dotted curve) of the demultiplexer as a function of frequency f for different values of $\delta = d_2 - d_1$ *and for* $d_0 = d_1 + d_2 =$ 8.57 *cm.*

Surprisingly, our coded version of the theory did not match the published results as shown in Figure 14. The published values had transmission resonances that were significantly narrower and the transmission away from resonance was significantly lower than our plots.

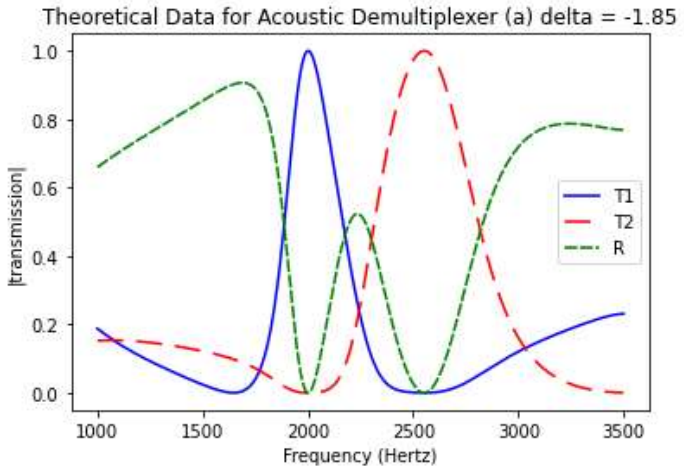

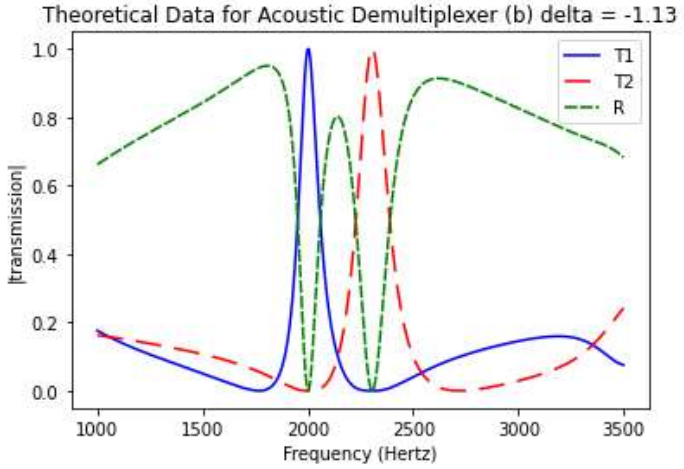

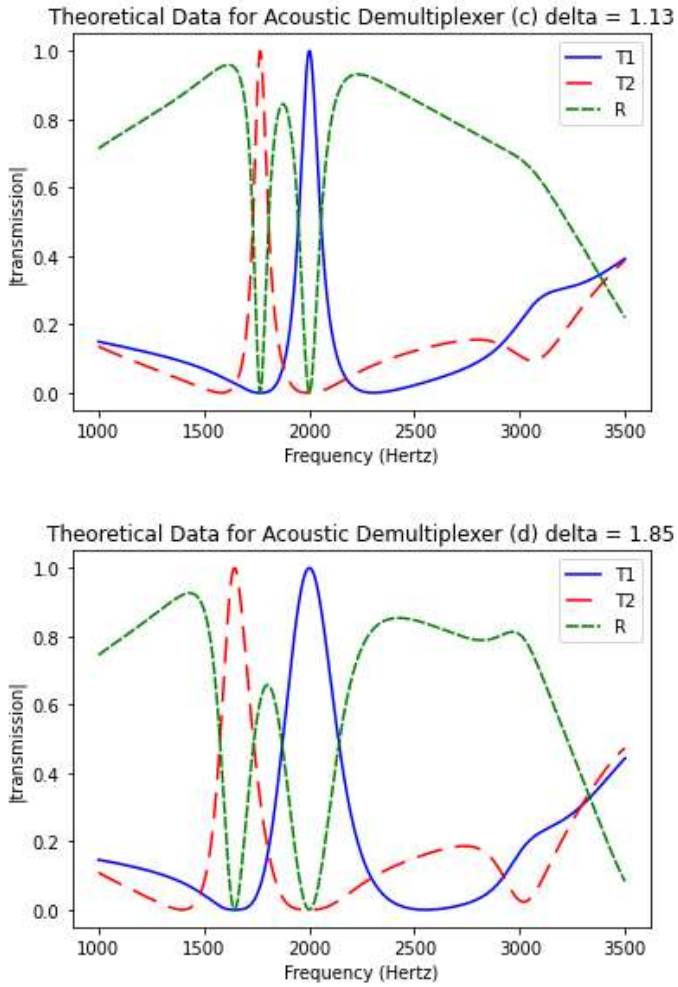

FIGURE 14: From the Python code: Variation of the transmission along the output 1 (continuous curve), the output 2 (discontinuous curve) and the reflection in the input (dotted curve) of the demultiplexer as a function of frequency f for different values of $\delta = d_2 - d_1$ *and for* $d_0 = d_1 + d_2 =$ 8.57 *cm.*

After some trials it appears that the results of Figure 13 of the reference plot $|t_1|^4$and $|t_2|^4$ versus frequency. These quantities correspond to intensity squared and do not have a ready physical interpretation.

We initially wanted to mimic experimentally the exact results of Figure 2(a)[4]

of the source work, where $d_0 = 8.57$ cm, $\delta = -1.85$ cm, and the lengths of d_1 -d_6 being $d_1 = 5.21$ cm, $d_2 = d_5 = 3.36$ cm, $d_3 = d_6 = 4.285$ cm, and $d_4 = 2.435$ cm. However, these dimensions were too small to 3D print and connect to polyvinyl chloride (PVC) pipe. So, we had to scale it up a bit. Given the dimension of the waveguide components and the audio frequency range that was best suited for our impulse response system for our experiment we used values of $d_0 = 25.71$ cm and $\delta = 1.85$ cm resulting in the lengths: $d_1 = 11.93$ cm, $d_2 = 13.78$ cm, $d_3 = 12.855$ cm, $d_4 = 14.705$, $d_5 = 13.78$, and $d_6 = 12.855$ cm. A plot of the analytic theory prediction of the transmitted intensity (T_1 and T_2 versus frequency) in each output arm is shown in Figure 15.

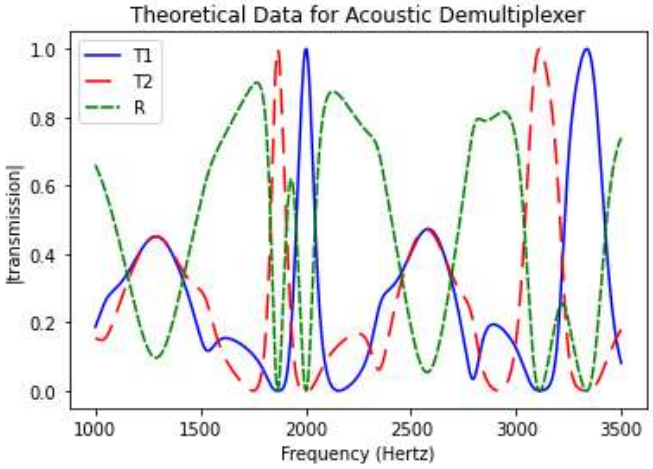

FIGURE 15: Transmission intensity for a Y-shaped demultiplexer: Simple analytic theory.

Over this frequency range there are two resonances in each arm resulting in perfect transmission. Figure 15 clearly shows that when the transmission along the first output (blue) reaches unity ($T_1 = 1$), the transmission along the second output T_2

(red) and the reflection R (green) vanish (i.e., $T_2 = R = 0$). Similarly, when the transmission along the second output line (red) reaches unity ($T_2 = 1$), the transmission along the first output line T_1 (blue) and the reflection R (green) vanish (i.e., $T_1 = R = 0$).

B. Experimental Configuration

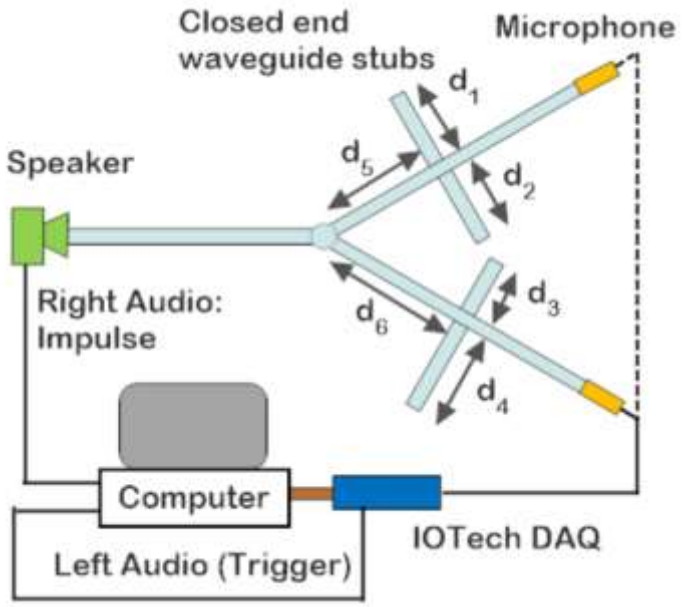

FIGURE 16: Schematic diagram of the impulse response system used to measure the transmission of the demultiplexer configuration. The key elements determining the selected frequencies for transmission are the side-loaded stub lengths (d_1-d_4) and their locations along the output arms (d_5, d_6).

A schematic of the experimental arrangement is shown in Figure 16 of the Y-shaped demultiplexer configuration. A small speaker (Apple M8756G/A) was connected at the input waveguide consisting of a 4.0 m long section of 2.0 cm diameter cylindrical acoustic waveguide made from PVC pipe. At the end of the input arm a 3D printed coupler was used to connect the two output waveguides. The angle between the output arms was approximately 60 degrees. Located along each output arm were a pair of side-loaded closed end waveguide stubs. Figure 16 shows the definition of the stub lengths (d_1 – d_4) and their location along the output arms

(d_5, d_6). These parameters define the frequencies that will be selectively transmitted down each output arm as specified in the published theory by Mouadilli [3]. The values of these parameters for the experiments described here were d_1 = 11.93 cm, d_2 = 13.78 cm, d_3 = 12.855 cm, d_4 = 14.705, d_5 = 13.78, and d_6 = 12.855 cm. To measure the frequency dependent transmission down each output arm a microphone (Aco Pacific 7012) was inserted into the end of the output arm. A computer sound card with stereo output was generated a short audio impulse on the right channel and a square trigger signal on the left channel. The short impulse signal was the second differential of a Gaussian function. The impulse was a directed to the speaker and the trigger signal to one analog-to-digital (AD) port of an IOTech DAQ/3000 data acquisition module. The DAQ/3000 was USB connected to the computer and, with each impulse, the audio signal transmitted to the microphone was digitally acquired at a second AD port. The use of triggered acquisition meant that each subsequent recorded impulse could be added and averaged coherently to the previous signals leading to time-domain data with very high signal-to-noise ratio. Typical runs used 200-400 averaged signal acquisitions. For more accurate measurement some runs used 1000 averaged signal acquisitions.

C. Finite Element Simulation

The finite element software COMSOL was used to numerically simulate the response of the Y-shaped demultiplexer. A 3D model of the system was created as shown in Figure 17.

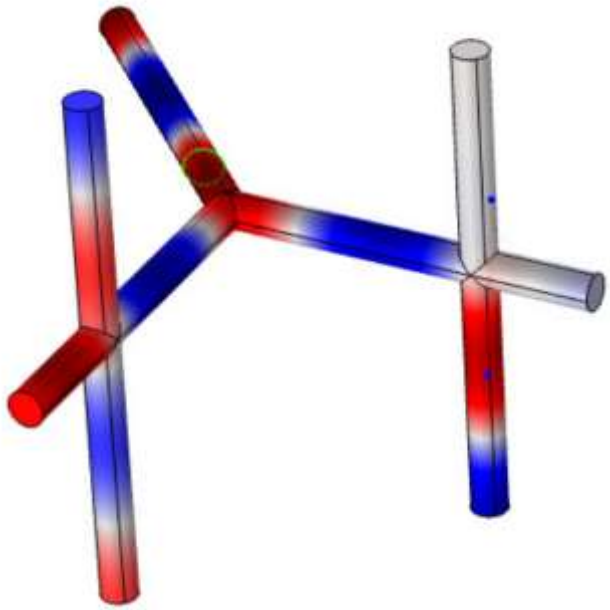

FIGURE 17: Pressure plot of the Y-shaped demultiplexer at 1900 Hz for which all the sound is channeled to one arm.

All of the surfaces were hard boundaries except for the end openings of the input and output arms. The input was a plane wave with amplitude of 0.2 Pa and the two output arms were impedance matched outputs such that there was no reflection from the end of each output arm. The input frequency was swept from 500 Hz to 3500 Hz in steps of 2 Hz. The output signal was determined by performing a surface integration of the acoustic intensity across each output face. The data were

normalized by running the simulation without the side loaded stubs and using the total integrated transmission at each output port as a reference. Notice that in Figure 17 the waveguide stubs are position horizontally and not vertically like the experimental set up. This is because in COMSOL the structure would combine the wave stubs together instead of constructing it at an angle.

D. Data Analysis

Before setting up the y-shaped demultiplexer, I would take a reference signal as shown in blue on Figure 12a by averaging hundreds of pulses down the straight pipe. To filter out the noise we use the add and average method, where after each pulse we add the measurements together and then divide by the number of pulses which averages out random noise. The time domain data is converted to the frequency domain using a numerical Fourier Transform as shown in Figure 12b. Numerical Fourier transforms were used to convert the time-domain data to the frequency domain. The frequency resolution of the Fourier transform (1 Hz) is limited by the need to truncate the acquired signal to eliminate back reflections from the ends of the waveguide. The combination of the 12 m long input waveguide and the two 12 m long output waveguide test bed assured that there was sufficient time before the first reflection to achieve good frequency resolution. [5]. The use of the straight waveguide data to normalize the y-shaped demultiplexer signal results in the transmission function of the structure alone, independent of loss, phase change, or detector response in the lead-in or lead-out waveguide system.

E. Experimental Results

The work explored with the acoustic Y-shaped demultiplexer arrangement proposed by Mouadili et al[1] was generally in excellent agreement between the finite element simulation and the experimental results as shown in Figure 18. The experimental transmission down each arm of the Y-shaped waveguide demultiplexer was measured using the impulse response technique described in the Experimental Configuration.

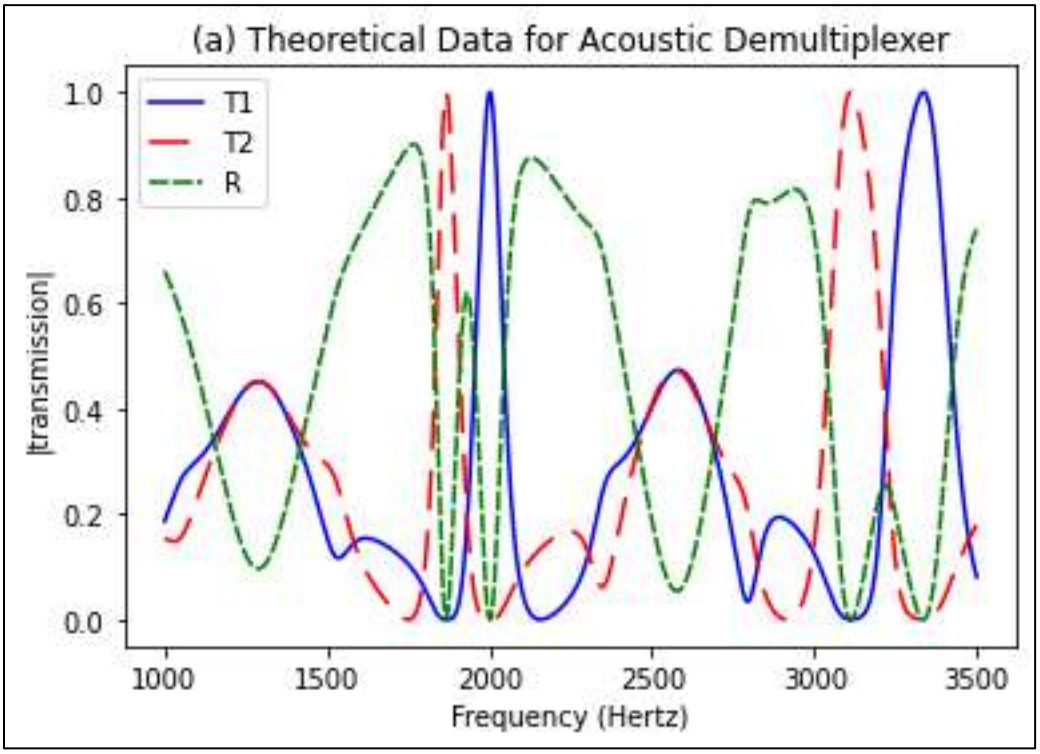

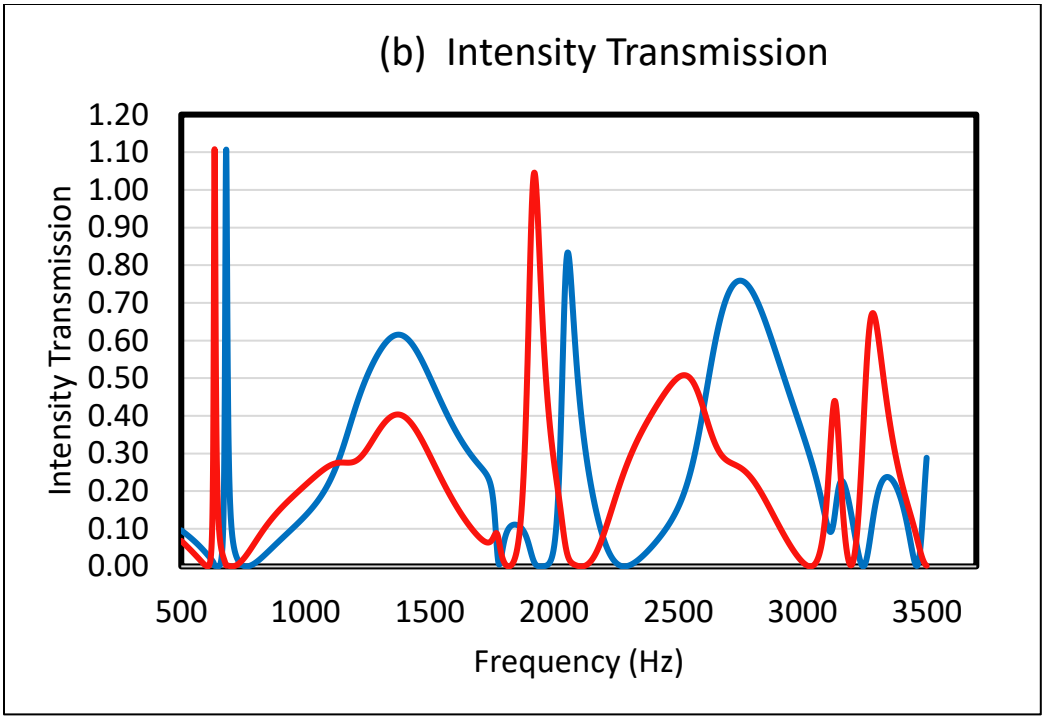

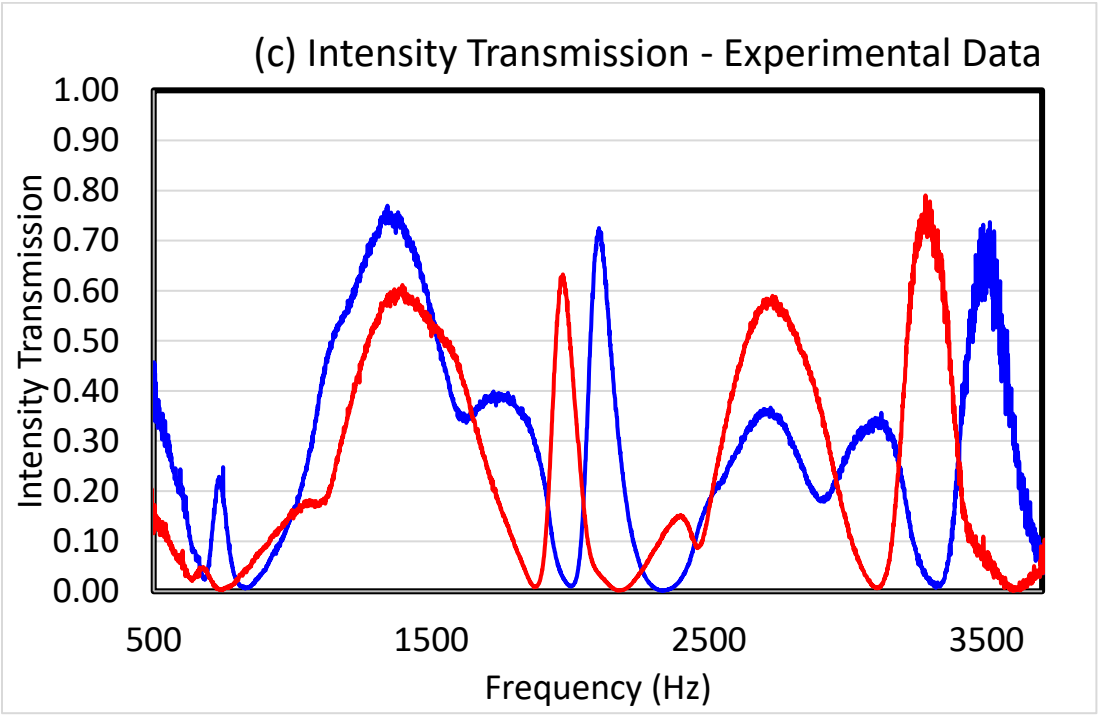

FIGURE 18: Transmission intensity for the Y-shaped Demultiplexer: (a) Simple analytic theory (b) Finite element simulation (c) Experimentally measured intensity transmission

The maximum transmission at resonance in this experiment is much lower than the theoretical or finite element predictions. However, this effect is primarily due to a limitation of the impulse response method in acoustic waveguide systems. Unlike the finite element simulation, there is no broad bandwidth impedance matching method for acoustic waveguides. In order to obtain data that are free from multiple reflections from the input and output ends of the waveguide it is necessary to truncate the time domain data. The effect of this truncation can be seen in the Figure 18c in which the sine-like oscillation of the signal continues beyond the truncation time. This effect is more pronounced for the narrowest resonances at low frequency. In contrast the broad bandwidth transmission away from resonance is roughly comparable to the predictions of theory and simulation.

To illustrate more directly the demultiplexing action of the system we created a narrow bandwidth pulse whose frequency matched the resonant frequency of one output arm and demonstrated that it is selectively sent down the appropriate arm. The pulse was created from a Gaussian envelope modulating a pure sine wave at the resonance frequency of one arm. The transmission of the pulse was then measured down the resonant and non-resonant arms of the demultiplexer. The result is shown in Figure 19.

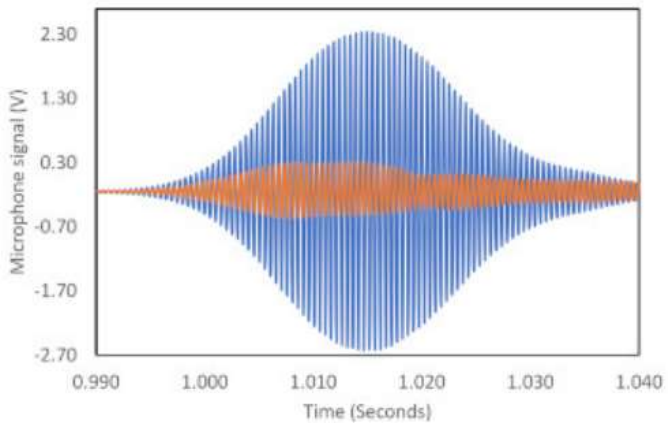

FIGURE 19: Transmission of an input Gaussian pulse of center frequency 2000 Hz down the resonant (blue) output arm and non-resonant (red) output arm of the demultiplexer.

The superposed signal down the resonant arm (blue plot) is much larger in amplitude and better retains its Gaussian shape compared to the weaker non-resonant arm signal (red plot).

F. Conclusions

This work explored the acoustic demultiplexer arrangement proposed by Mouadili et al. [1]. Finite element simulations show good agreement with the theory and the impulse response and direct pulse experiments agree well qualitatively. However, neither matches identically with the theoretical model. The experimental data peaks do not achieve the perfect transmission predicted in both the theoretical analysis and the COMSOL simulation. Such differences likely occur as a result of the computational and theoretical models failing to account for absorption and energy loss in transmission. However, the impulse method truncates the transmission signal and could fail to fully capture the narrow frequency output. The practical use of such a multiplexer for acoustic waveguides is limited although there are potential uses in gas transport pipelines where acoustic wave buildup can require suppression. The main value is that analogous arrangements using Fano-resonance mediated wave manipulation is finding application in other more practical systems such as optical metasurfaces or coaxial cable electrical filters. The results of this work were published in AIP Advances [7].

XI. REFERENCES

1. Rabus, Dominik Gerhard. *"*Integrated Ring Resonators: The Compendium." *Springer International Publishing*, (2007).

2. Vasseur, A. Akjouj, L. Dobrzynski, B. Djafari-Rouhani, E.H. El Boudouti, Surf. Sci. Rep. 54, 1 (2004).

3. A. Mouadili, E.H. El Boudouti, A. Soltani, A. Talbi, K. Haddadi, A. Akjouj, B. Djafari-Rouhani, J. Phys. D 52, 075101 (2019).

4. A. Mouadili et al.: Eur. Phys. J. Appl. Phys. 90, 10902 (2020).

5. W. M. Robertson and J. M. Parker, J. Acoust. Soc. Am. 131, 2488–2944 (2012).

6. W. M. Robertson, C. Vazquez, A. LaVerde, A. Wassenberg, C. Olson, J. Lopez. AIP Advances 12, 015006 (2022); https://doi.org/10.1063/5.0077330

7. W. M. Robertson, C. Vazquez, J. Lopez, A. LaVerde, R.J. Giuntini. AIP Advances 12, 045018 (2022); https://doi.org/10.1063/5.0087034